PNAS

Main Manuscript for

Emergence of Bulk-Like Structural Features and 2D-to-3D Transition in Boron Nanoclusters

Qiang Chen[a,1], Hyun Wook Choi[b,1], Guang-Feng Wei[c,1], Deniz Kahraman[b], Rui-Nan Yuan[a], Qin-Wei Zhang[a], Qiao-Qiao Yan[a], Xiao-Ni Zhao[a], Cai-Yue Gao[a], Yuan-Yuan Ma[d], Rui Wei[a], Yilin Gui[c], Zhi-Pan Liu[e,2], Si-Dian Li[a,2], and Lai-Sheng Wang[b,2]

[a]Institute of Molecular Science, Shanxi University; Taiyuan 030006, China

[b]Department of Chemistry, Brown University; Providence, RI 02912, USA

[c]Shanghai Key Laboratory of Chemical Assessment and Sustainability, School of Chemical Science and Chemical Engineering, Tongji University, Shanghai 200092, China

[d]Department of Energy Chemistry and Materials Engineering, Shanxi Institute of Energy, Jinzhong 030600, China

[e]Department of Chemistry, Fudan University, Shanghai 200433, China

[1]These authors contributed equally to this work

[2]To whom correspondence should be addressed: Zhi-Pan Liu; Si-Dian Li; Lai-Sheng Wang,

Email: zpliu@fudan.edu.cn; lisidian@sxu.edu.cn; lai-sheng_wang@brown.edu

Author Contributions: L.S.W., S.D.L., Z.P.L., and Q. C. conceived the idea and finalized the manuscript. L.S.W. supervised the PES experiment. S.D.L. supervised the theoretical work. Q.C. supervised the chemisorption experiment. H.W.C. and D. K. performed the PES experiment. G.F.W., Y.G., and Z.P.L. performed the SSW GM search. G.F.W., R.N.Y., Q.W.Z., Q.Q.Y., X.N.Z., C.Y.G., Y.Y. M, and R.W. performed the theoretical calculations. L.S.W. and S.D.L. co-wrote the paper. All authors contributed to the discussion and commented on the manuscript.

Competing Interest Statement: The authors declare no competing interest.

Classification: The major classification: Physical Sciences; The minor classification: Chemistry

Keywords: boron cluster; chemisorption; photoelectron spectroscopy; structural transition; computational chemistry.

This PDF file includes:

Main Text
Figures 1 to 6

Abstract

As an electron-deficient element, boron possesses fascinating three-dimensional structures and unconventional chemical bonds. Nanoclusters of boron have also been found to exhibit intriguing structural properties, observed to have predominantly planar structures, in stark contrast to bulk boron allotropes, which are composed of the ubiquitous B_{12} icosahedral building blocks. Here we report observation of the 2D-to-3D transition and bulk-like structural features in the size-selected boron clusters, as revealed by photoelectron spectroscopy, chemisorption experiments, and first-principles calculations. In the small to medium cluster size range, planar boron cluster anions are found to be unreactive and only B_{46}^- and B_{56}^- are observed to chemisorb C_2H_4 and CO under ambient conditions, suggesting major structural transitions at these cluster sizes. Notably, B_{56}^- is also found to be able to chemisorb and activate CO_2. The global minimum of B_{46}^- is found to adopt a core-shell configuration ($B_2@B_{44}^-$), consisting of a B_2 core encapsulated within a B_{44} shell, reminiscent of the interstitial B_2 dumbbells in the high-pressure γ-B_{28} form of bulk boron. More remarkably, both the global minimum and second most stable isomer of B_{56}^- exhibit nest-like configurations ($B_{12}@h$-B_{44}^-), featuring the iconic B_{12} icosahedral core surrounded by a B_{44} half-shell, signifying the onset of bulk-like structural characteristics in boron nanoclusters.

Significance Statement

Investigation of the size-dependent properties in nanoclusters laid the foundation for nanoscience. Boron clusters are found to be planar, leading to the discovery of borophenes – a new class of synthetic 2D-materials. A long-sought question in boron cluster research is: at what size does the 2D-to-3D transition occur, or more pertinently, at what size does the defining bulk-like B_{12} icosahedral cage emerge? This study shows that the 2D-to-3D transition occurs at B_{46}^-, which exhibits a core-shell structure, while the B_{56}^- cluster is found to incorporate the iconic B_{12} icosahedral unit inside a B_{44}-half-shell. These findings serve as important milestones in understanding the structural evolution of boron nanoclusters and their potential applications in chemistry and materials science.

Main Text

Introduction

Atomic clusters display size-dependent properties, forming the foundation of nanoscience. The investigation of atomic clusters has resulted in the discoveries of fullerenes (1), that led to carbon nanotubes and graphene (2, 3), and the electron shell model (4), that underlies the concept of superatoms (5). One of the most important questions in the investigation of atomic clusters is how bulk-like structural properties emerge as a function of size. For example, small carbon clusters form sp-hybridized chains and rings up to C_{20}, at which point sp^2-hybridized fullerene cage and bowl-shaped aromatic structures appear (6), which are akin to graphite. Carbon's lighter neighbor, boron, has many different allotropes (7), all consisting of polyhedral cages, in particular the ubiquitous B_{12} icosahedral cage. However, joint experimental and theoretical studies have shown that size-selected boron clusters are predominantly planar up to 42 atoms (*SI Appendix*, Fig. S1) (8–11), with the exception of the B_{40} and B_{39}^- borospherene cages (12, 13). The discovery of the planar B_{36} cluster provided the first experimental evidence for the viability of borophenes (14), which have been synthesized on inert substrates and are becoming a new class of synthetic 2D materials (15, 16). A long-sought question in boron cluster research is: at what size does the 2D-to-3D transition occur or more pertinently at what size does the defining bulk-like B_{12} icosahedral cage emerge?

Theoretical calculations using density functional theory (DFT) have indicated 3D structures and B_{12}-containing core-shell structures in large boron clusters (17–21). The bulk-like B_{12} motif was first suggested to be at the core of high symmetry stuffed fullerene-like core-shell boron clusters (B_{84}, B_{98}, B_{100}, B_{102}) (17). The most stable structure of the B_{80} cluster was subsequently found to be low symmetry core-shell structures containing the B_{12} motif (18-20). The B_{46} cluster was suggested by DFT calculations to be a 3D boron cluster with a B_4 core-shell structure ($B_4@B_{42}$) (22). A recent DFT study suggests that B_{56} favors a single-B core-shell structure ($B@B_{55}$) and B_{58} is the smallest boron cluster containing a B_{12} core and a 46-atom half-shell ($B_{12}@h\text{-}B_{46}$) (23). However, none of the 3D or core-shell structures has been experimentally verified. The principle experimental technique that has been used to probe the structures and bonding of boron clusters has been photoelectron spectroscopy (PES) of size-selected cluster anions (B_x^-) (9), but photoelectron spectra of large B_x^- clusters are becoming more congested with less fingerprint electronic signatures for definitive structural determination. The largest cluster that has been solved by PES and theoretical calculations is B_{48}^- (24), which was found to possess a bilayer structure. The challenges that have plagued PES for large boron clusters are the difficulty to create cold clusters and the possibility of coexisting isomers. Clearly, other experimental techniques that can provide additional structural information would be essential to make progress to solve the mystery of large boron clusters. Though ion mobility, which is capable of providing structural information for size-selected clusters, was applied to small boron cluster cations (B_x^+, $x \leq 25$) (25), it was not feasible for any B_x^- clusters due to weak anionic cluster signals and collision-induced electron detachment.

Here we combine PES with chemisorption experiment to probe the 2D-to-3D structure transition in boron nanoclusters. We expect that 2D boron cluster anions should be less reactive because of the strong peripheral B–B bonds and the smooth planar surfaces (8–11), whereas 3D structures with more rugged surfaces may provide reactive sites for chemisorption. Intriguingly, we find that in the small to medium size range and under ambient conditions, only B_{46}^- and B_{56}^- can chemisorb C_2H_4 and CO, whereas B_{56}^- can also chemisorb CO_2, even partially releasing CO to form $B_{56}O^-$. Kinetic studies show that there are at least two isomers co-existing for B_{46}^-, one of which does not chemisorb C_2H_4 or CO. The B_{56}^- cluster is found in the kinetic study to have at least three low-lying isomers, one of which can chemisorb one CO_2 molecule and another can react with CO_2 to form $B_{56}O^-$ by releasing a CO molecule. PES in combination with theoretical calculations reveals that the lowest energy structure of B_{46}^- consists of two degenerate core-shell isomers, a C_2 $B_2@B_{44}^-$ (**1**) and a C_1 $B@B_{45}^-$ (**2**) competing for the global minimum (GM), along with two low-lying core-shell isomers, C_1 $B@B_{45}^-$ (**3**) and C_1 $B@B_{45}^-$ (**4**). The rough surfaces of the core-shell structures are found to provide chemisorption sites for C_2H_4 and CO, although the major isomer C_2 $B_2@B_{44}^-$ (**1**) is found to have a large reaction energy barrier on the adsorption pathway. The GM of B_{56}^- is found to possess a nest-like C_1 $B_{12}@h\text{-}B_{44}^-$ (**5**) structure, consisting of an unprecedented B_{12} icosahedral core and a 44-atom half-shell, followed by another nest-like C_s $B_{12}@h\text{-}B_{44}^-$ (**6**) isomer, along with a single-B core-shell C_{3v} $B@B_{55}^-$ (**7**) and a bilayer C_1 B_{56}^- (**8**). The two nest-like structures, C_1 $B_{12}@h\text{-}B_{44}^-$ (**5**) and C_s $B_{12}@h\text{-}B_{44}^-$ (**6**), and the bilayer B_{56}^- (**8**) can chemisorb C_2H_4, CO, and a single CO_2 molecule, while in particular, the bilayer structure (**8**) with a unique interfacial pentagonal active site can activate CO_2 to further form $B_{56}O^-$ + CO under ambient conditions. Thus, the B_{46}^- cluster defines the 2D-to-3D transition and the B_{56}^- cluster marks the onset of bulk-like structural features in boron nanoclusters.

Results

Chemisorption with C_2H_4, CO, and CO_2. We produced boron clusters using laser vaporization of a ^{11}B-enriched target and conducted the chemisorption experiment in a downstream linear ion trap under ambient conditions (26) (see *SI Appendix* and *SI Appendix,* Fig. S2 for details). Fig. 1A displays the B_x^- (x = 10–68) cluster distributions upon reactions with C_2H_4, CO, and CO_2 using He as a reference (top). Upon filling the ion trap with 0.06 Pa C_2H_4 with a 2 ms reaction time, the cluster distribution exhibits no notable change for x<57, except B_{46}^- and B_{56}^-: their relative intensities are significantly reduced with the concurrent appearance of the $B_{46}(C_2H_4)^-$ and $B_{56}(C_2H_4)^-$ products. The B_{55}^- cluster also shows a slight intensity reduction, along with a weak $B_{55}(C_2H_4)^-$ product, whereas clusters larger than B_{58}^- all seem to exhibit reactivity with C_2H_4. Similar reaction patterns are observed for CO, except that the reactivity with CO appears to be much weaker than with C_2H_4, so that a higher CO partial pressure (0.15 Pa) and a longer reaction time (8 ms) are used. Most remarkably, we find that only B_{56}^- is reactive with CO_2 to produce $B_{56}(CO_2)^-$ in the entire cluster size range from B_{10}^- to B_{68}^-. These observations suggest that both B_{46}^- and B_{56}^- are likely to have 3D structures with surface chemisorption sites and B_{56}^- must have a very special structure to be able to chemisorb CO_2.

We conducted size-selected chemisorption experiments to examine the reaction products and kinetics by turning on the quadrupole mass filter before the ion trap (*SI Appendix*, Fig. S2). We find that B_{46}^- can chemisorb up to six C_2H_4 and two CO molecules under ambient conditions (Fig. 1B), while B_{56}^- can chemisorb up to six C_2H_4 and four CO molecules (Fig. 1C). Only one CO_2 molecule is observed to chemisorb onto B_{56}^-, while, surprisingly, a weaker $B_{56}O^-$ product is also observed, indicating that B_{56}^- can react with CO_2 to spontaneously release a CO. Using least-squares fitting, we estimated the pseudo-first-order rate constants k_1 (in cm^3 $molecule^{-1}$ s^{-1}) of the following six chemisorption processes, as given in Fig. 1B and 1C (right) (see *SI Appendix*):

$$B_{46}^- + nC_2H_4 \rightarrow B_{46}(C_2H_4)_n^- \quad (n = 1\sim3) \quad k_1 = 4.07\times10^{-11} \qquad (1)$$

$$B_{46}^- + nCO \rightarrow B_{46}(CO)_n^- \quad (n = 1\sim2) \quad k_1 = 7.77\times10^{-13} \qquad (2)$$

$$B_{56}^- + nC_2H_4 \rightarrow B_{56}(C_2H_4)_n^- \quad (n = 1\sim6) \quad k_1 = 5.57\times10^{-11} \qquad (3)$$

$$B_{56}^- + nCO \rightarrow B_{56}(CO)_n^- \quad (n = 1\sim4) \quad k_1 = 2.42\times10^{-12} \qquad (4)$$

$$B_{56}^- + CO_2 \rightarrow B_{56}(CO_2)^- \quad k_1 = 7.88\times10^{-13} \qquad (5)$$

$$B_{56}^- + CO_2 \rightarrow B_{56}O^- + CO \quad k_1 = 1.50\times10^{-13} \qquad (6)$$

The reactivities of both B_{46}^- and B_{56}^- with CO appear to be much weaker than with C_2H_4, while the production of $B_{56}O^-$ is the slowest reaction in the series, as shown in their estimated pseudo-first-order rate constant k_1. More significantly, the kinetic studies reveal that there are at least two isomers for B_{46}^-. Only the minor isomers are reactive with C_2H_4 and CO, contributing 36% and 37% to the total population for B_{46}^-, respectively (Fig. 1B). Both the C_2H_4 and CO reaction kinetics for B_{56}^- show that 58% of the cluster population is reactive, while 42% is unreactive toward both C_2H_4 and CO (Fig. 1C). However, the CO_2 kinetic experiment reveals that there are at least three isomers in the B_{56}^- cluster beam (Fig. 1C): One isomer (48%) chemisorbs one CO_2, while another minor isomer (9%) can spontaneously react with CO_2 to form $B_{56}O^-$. Apparently, both isomers can

chemisorb C_2H_4 and CO because the inert isomer population (42~43%) remains basically unchanged in the C_2H_4, CO, and CO_2 chemisorption experiments, as shown in Fig. 1C.

Global Minimum Searches for B_{46}^- and B_{56}^-. We used the stochastic surface walking (SSW) method (27) in conjunction with manual structural construction to search for the global minima of B_{46}^- and B_{56}^- (see *SI Appendix* for details). The four lowest-lying isomers for each cluster are shown in Fig. 2 (see *SI Appendix*, Table S1 for the coordinates and Fig. S3 for more isomers). At the DLPNO-CCSD(T) level of theory for both the relative electronic energies (ΔE) at 0 K and the Gibbs free energies (ΔG) at 298 K, the GM structure of B_{46}^- consists of two degenerate core-shell isomers, $B_2@B_{44}^-$ (**1**) and $B_1@B_{45}^-$ (**2**) with C_2 and C_1 symmetries, respectively (Fig. 2A). The C_2 isomer **1** consists of a B_2 core and a 44-atom shell ($B_2@B_{44}^-$) (see the 3D structure), with two apex atoms on the top and bottom each capping a B_4 square, which is connected to two filled concave hexagons and two unfilled hexagons. The equator of the C_2 $B_2@B_{44}^-$ consists of two filled concave pentagons, two unfilled pentagons, and four filled convex pentagons, giving rise to four somewhat protruding surface atoms. The two core B atoms are bonded to each other, as well as four surface atoms each, two of which are the center atoms of the two filled concave hexagons. Each of the core B atoms is also bonded to the same two center atoms from two filled concave pentagons on the equator to give rise to the C_2 symmetry.

The degenerate C_1 isomer **2** consists of a single B atom core with a B_{45} shell ($B@B_{45}^-$), which is similar to the B_{44} shell of isomer **1** except that in isomer **2** there are three filled concave hexagons connected to each of the apex square pyramid (see the 3D structure). On the equator of isomer **2**, there are three unfilled pentagons, four filled convex pentagons, and one filled concave pentagon. The core B atom of isomer **2** is bonded to six B atoms, five of which are the center atoms of five concave hexagons and one of which is bonded to the center B atom of one of the concave pentagons on the equator. There is another low-lying C_1 isomer **3**, which is 0.12 eV higher in energy than the GM at DLPNO-CCSD(T). Isomer **3** ($B@B_{45}^-$) also consists of a single core atom and its B_{45} shell is almost identical to that of isomer **2** (see the 3D structure). The minor differences between **2** and **3** originate from the slight structural relaxations in the C_1 coordination environment of the core atom. A similar situation happens to the core-shell C_1 $B@B_{45}^-$ isomer **4**.

As the well-defined GM of the system, B_{56}^- (**5**) (Fig. 2B) is nest-like, consisting of a B_{12} icosahedral core and a 44-atom half-shell ($B_{12}@h\text{-}B_{44}^-$) with C_1 symmetry. The GM $B_{12}@h\text{-}B_{44}^-$ (**5**) is found to be 0.47, 0.72, and 1.12 eV more stable than the second nest-like C_s $B_{12}@h\text{-}B_{44}^-$ (**6**), the single-B core-shell C_{3v} $B@B_{55}^-$ (**7**), and the bilayer C_1 B_{56}^- (**8**) at DLPNO-CCSD(T), respectively (see the 3D structures). With the entropy effects included at room temperature (298 K), the GM **5** lies 0.38, 0.79, and 0.90 eV more stable than **6**, **7**, and **8** in Gibbs free energies at the same level of theory, respectively. The C_1 $B_{12}@h\text{-}B_{44}^-$ (**5**) GM is remarkable: three B atoms on the top of the bulk-like B_{12} core are completely exposed, six are at the interface with the half-shell, and three are completely inside the half-shell, each forming one B–B bond with a center atom of a filled concave hexagon on the B_{44} half-shell. The second nest-like isomer, $B_{12}@h\text{-}B_{44}^-$ (**6**), possesses a similar structure with C_s symmetry. The half-shells are somewhat smoother, in comparison with the surfaces of the four low-lying isomers of B_{46}^- (Fig. 2**A**). There exist two unfilled adjacent pentagons at the bottom and one isolated pentagon on the waist of the half-shell in the GM C_1 $B_{12}@h\text{-}B_{44}^-$ (**5**) and two unfilled adjacent pentagons symmetrically distributed at the bottom of the half-shell in C_s $B_{12}@h\text{-}B_{44}^-$ (**6**), whereas the rest of the surface consists of filled hexagons and pentagons. At the interface between the B_{12} core and the B_{44} half-shell, we find one B_3 triangle, four B_5 pentagons, and two B_6 hexagons in the GM $B_{12}@h\text{-}B_{44}^-$ (**5**) and two B_3 triangles, four B_5

pentagons, and two B_6 hexagons in the B_{12}@*h*-B_{44}^- isomer **6** (see the 3D structure). Unlike other bilayer structures, such as the bilayer B_{48}^- cluster (24), the bilayer isomer of B_{56}^- (**8**) possesses one B_5 pentagon at the lower right corner (see the 3D structure) to serve as the active site at the interface between the two layers, which is also the reactive site for C_2H_4, CO, and CO_2 (*vide infra*).

While there were prior calculations on neutral B_{46} and B_{56}, there were no computational studies on their anions. A recent DFT study suggested a core-shell B_{46} (B_2@B_{44}) similar to B_{46}^- (**1**) (22), a core-shell B_{56} (B@B_{55}) similar to B_{56}^- (**7**) (23), and a bilayer C_1 B_{56} similar to B_{56}^- (**8**) (28). The GM structures identified for B_{46}^- (**1**) and B_{56}^- (**5**) need to be verified by PES and should explain the observed chemisorption properties. To that end, the vertical detachment energies (VDEs) for the four lowest energy isomers of each cluster are computed, as well as their adiabatic detachment energies (ADEs) (*SI Appendix*, Table S2).

Photoelectron Spectroscopy of B_{46}^- and B_{56}^- and Comparison with Simulated Spectra. PES has been the most powerful experimental technique to investigate size-selected boron clusters (*9*). The structures and bonding of boron clusters up to B_{42}^- (*SI Appendix*, Fig. S1) along with the bilayer B_{48}^- have been elucidated by PES in conjunction with theoretical chemistry (8–14). However, with increasing cluster size, it becomes challenging to obtain PES data with well-resolved features primarily due to the difficulty to produce cold clusters as a result of the large heat of formation. To enhance the cooling of large clusters, we have tested helium carrier gas seeded with different amounts of Ar, which is expected to be a more efficient collision partner with large clusters (see *SI Appendix* for more experimental details). As shown in *SI Appendix*, Fig. S4, we find that pure He carrier gas gives essentially featureless photoelectron spectra for B_{46}^- and B_{56}^-, while better resolved spectra are obtained with higher percentage of Ar in the carrier gas. We find that 15% Ar gives the optimal results, while no significant improvement is found with 20% Ar. The 193 nm spectra measured using the 15% Ar-seeded He carrier gas are compared in Fig. 3 with the simulated spectra for the GM structures and the three low-lying isomers of B_{46}^- and B_{56}^-. We also obtained the photoelectron spectra of B_{46}^- and B_{56}^- at 266 nm, which are slightly improved, but largely confirm the resolved features in the 193 nm spectrum (*SI Appendix*, Fig. S5).

Both spectra are quite congested, suggesting that there may be multiple isomers in the cluster beam. Discernible features and their VDEs are labeled on the experimental spectra for the sake of discussion and are also given in Table S2. In the spectrum of B_{46}^- (Fig. 3A), the weak X band at a VDE of 3.38 eV followed by a large energy gap is characteristic of a closed-shell neutral B_{46} cluster with a sizable HOMO-LUMO gap, defined by bands X and B. The shoulder A at 4.04 eV appears to be from another isomer. The computed ADE/VDE1 (*SI Appendix*, Table S2) and the simulated spectral pattern for the GM structure **1** are in good agreement with the experimental data. Its large HOMO-LUMO gap confirms that band A is indeed from another isomer. The degenerate isomer **2** gives a higher computed ADE and VDE1 (*SI Appendix*, Table S2), which could account for the observed signals in the HOMO-LUMO gap region of structure **1**, including band A. Isomers **3** and **4** yield similar simulated spectra (Fig. 3A) as isomer **2**, due to their similar core-shell structures. While isomers **3** and **4** probably cannot be ruled out, their populations are expected to be much smaller on the basis of their relative energies (Fig. 2A). The simulated spectra of isomers **2** and **3** do not reveal a HOMO-LUMO gap, because their neutrals all have triplet ground states. The large HOMO-LUMO gap for the GM structure **1** suggests that its corresponding neutral is highly stable electronically. The B_{46}^- cluster is thus the first boron cluster observed to date to consist of core-shell type structures, representing a major structural change from the 2D or cage structures found in smaller B_x^- clusters (*SI Appendix*, Fig. S1).

The photoelectron spectrum of B_{56}^- is even more complicated and less resolved, showing two weak overlapping bands X and A (Fig. 3B) in the low binding energy region. The computed VDE1 for the GM nest-like B_{12}@*h*-B_{44}^- structure **5** and those for isomers **6**, **7**, **8** are similar (*SI Appendix*, Table S2), contributing to the broad band X. All four isomers are closed-shell in their neutral forms, giving rise to a HOMO-LUMO gap in the simulated spectra of the anion. Isomers **5** and **7** have smaller HOMO-LUMO gaps, and the second bands in their simulated spectra agree well with band A. Isomers **6 and 8** have slightly larger HOMO-LUMO gaps and their second detachment bands agree well with band B. The complexity of the measured photoelectron spectrum is likely the result of the presence of four low-lying isomers in the cluster beam of B_{56}^-. The GM nest-like C_1 B_{12}@*h*-B_{44}^- (**5**) and the second lowest-lying nest-like C_s B_{12}@*h*-B_{44}^- (**6**) with an icosahedral B_{12} core are remarkable, suggesting the onset of bulk-like features in size-selected boron clusters.

The presence of low-lying isomers revealed by PES of the B_{46}^- and B_{56}^- clusters is consistent with the chemisorption experiments which suggest that there are at least two isomers present for B_{46}^- (Fig. 1B) and three isomers for B_{56}^- (Fig. 1C). The validity of the core-shell global minima and the low-lying isomers for B_{46}^- and B_{56}^- can be further examined through the chemisorption mechanisms with C_2H_4 and CO, as well as CO_2 in the case of B_{56}^-.

Mechanisms of C_2H_4 and CO Chemisorption on B_{46}^- and B_{56}^-. We consider the chemisorption mechanisms onto the three lowest-lying isomers of B_{46}^- and the four lowest-lying isomers of B_{56}^- by the first C_2H_4 and CO molecules in Fig. 4. We find that both isomers **2** and **3** of B_{46}^- exhibit no energy barriers at the transition states (**TS3** and **TS4**) in their most favorable top-adsorption sites, leading to the $B_{46}(C_2H_4)^-$ products **I5** and **I7** with chemisorption energies (E_{cse}) of 2.92 eV and 3.06 eV at DLPNO-CCSD(T), respectively (Fig. 4A). On the other hand, there is a large energy barrier of +0.87 eV (**TS1**, Fig. 4A) for the C_2H_4 adsorption onto the GM structure **1**, which is thus unlikely to react with C_2H_4 at ambient conditions. Hence, isomers **2** and **3** should be responsible for the observed minor population of B_{46}^- (36%), that is reactive toward C_2H_4, whereas the GM isomer **1** accounts for the major unreactive population of B_{46}^- found in the kinetic study (64%) (Fig. 1B). The first C_2H_4 chemisorbs on the most protruding top apex B atom of B@B_{45}^- for both isomers **2** and **3** along with a neighboring boron atom on the B_4 square (Fig. 4A and the 3D structure). The π bond in $H_2C{=}CH_2$ is broken, forming two C–B σ bonds and resulting in the large chemisorption energies for **I5** and **I7** (Fig. 4A). Alternative C_2H_4 chemisorption sites are computed for isomer **2**, which are all less favorable relative to **I5** (*SI Appendix*, Fig. S6A). In contrast, for the GM isomer **1,** the first C_2H_4 favors the apex atom on the convex pentagon at the equator along with a periphery boron atom in an unfilled hexagon (see the 3D structure). In addition to the large reaction barrier of +0.87 eV, the chemisorption energy for isomer **1** (2.36 eV) is also obviously smaller than that for isomers **2** and **3** (Fig. 4A). The CO chemisorption behaviors on the isomers of B_{46}^- are similar to those of C_2H_4. Isomers **2** and **3** of B_{46}^- exhibit barrierless adsorption to the bottom apex atom (Fig. 4B) and they should be responsible for the reactive population (37%) observed in the kinetic study (Fig. 1B). The GM isomer **1** displays a sizable energy barrier of +0.10 eV (**TS5**) and a relatively small chemisorption energy for CO adsorption (0.82 eV), consistent with the unreactive population of B_{46}^- (63%, Fig. 1B). The chemisorption energies for CO for both isomers **2** and **3** are much smaller than those for C_2H_4, in agreement with the lower CO reactivity found in the kinetic study (Fig. 1B). We also computed the successive chemisorption by C_2H_4 and CO onto isomer **2** of B_{46}^- to form $B_{46}(C_2H_4)_n^-$ (n = 1–6) and $B_{46}(CO)_n^-$ (n = 1, 2). We find that the chemisorption energies increase linearly with the number of adsorbed molecules with $E_{cse} = 2.41n + 0.51$ (*SI Appendix*, Fig.

S7A) and E_{cse} = 1.59*n* + 0.04 (*SI Appendix*, Fig. S7B) for C_2H_4 and CO, respectively. The linearity of the chemisorption energies suggests that the chemisorption does not change the core-shell structure of the B_{46}^- cluster significantly.

For C_2H_4 chemisorption on B_{56}^-, we find that both the nest-like GM B_{12}@*h*-B_{44}^- (**5**) and the second nest-like isomer B_{12}@*h*-B_{44}^- (**6**) exhibit no reaction barriers (**TS6** and **TS7** in Fig. 4C) and large adsorption energies of 2.64 and 2.65 eV to form $B_{56}(C_2H_4)^-$ (**I13**) and $B_{56}(C_2H_4)^-$ (**I15**), respectively. The B@B_{55}^- isomer **7** with a more smooth B_{55} shell shows a large reaction barrier of +0.43 eV, as well as a relatively small chemisorption energy (1.80 eV, Fig. 4C). The bilayer isomer **8** displays no energy barrier to form $B_{56}(C_2H_4)^-$ with a large adsorption energy of 2.48 eV. Thus, the nest-like isomers **5** and **6** and bilayer isomer **8** should account for the 58% reactive population of B_{56}^-, whereas the B@B_{55}^- isomer **7** is responsible for the 42% unreactive population found in the kinetic study with C_2H_4 (Fig. 1C). The C_2H_4 molecule is adsorbed on the exposed B_3 triangle of the B_{12} core of the GM isomer **5** (see the 3D structure) in a top-adsorption mechanism, resulting in the breaking of the H_2C=CH_2 π bond and the formation of two C–B σ bonds (Fig. 4C). We also considered other chemisorption sites (*SI Appendix*, Fig. S6C): in addition to the top B_3 site, the sites at the interface between the B_{12} core and the B_{44} half-shell are also good adsorption sites, whereas all the other sites are much less favorable. The C_2H_4 molecule chemisorbs on the interfacial pentagonal site of the bilayer isomer **8**, breaking the H_2C=CH_2 π bond and forming two C–B σ bonds spontaneously (see the 3D structure). The CO chemisorption behaviors among the low-lying isomers of B_{56}^- are similar to those of C_2H_4, as shown in Fig. 4D. Both the nest-like **5** and **6** and bilayer **8** isomers exhibit no energy barriers to adsorb a CO, and they should be responsible for the population of B_{56}^- (58%), that is reactive with CO (Fig. 1C). The core-shell B@B_{55}^- isomer **7** with a smooth shell displays a sizable energy barrier of +0.21 eV (**TS11**) and relatively small adsorption energy of 0.64 eV for adsorption of CO, and it should correspond to the unreactive population of B_{56}^- (42%). The relatively high percentage of isomer **7** could indicate a kinetic trapping. The preferential formation of this relatively high energy isomer is probably due to two reasons: 1) the preference of smaller boron clusters to form 2D structures and (2) the relative inertness of isomer **7** that may help its survival during the cluster growth. The chemisorption energies of CO on B_{56}^- isomers are significantly smaller than those for the C_2H_4 adsorption, consistent with the lower CO reactivity (Fig. 1C). Interestingly, the first CO molecule chemisorbs on a B atom of the B_{44} half-shell at the interface with the B_{12} core (Fig. 4D and the 3D structure). We also explored adsorption sites of CO on the GM isomer **5** of B_{56}^- and found that the interface sites all give similar chemisorption energies (*SI Appendix*, Fig. S6D). We considered the consecutive C_2H_4 and CO adsorption on the GM nest-like B_{12}@*h*-B_{44} isomer **5** to form $B_{56}(C_2H_4)_n^-$ (*n* = 1–6) and $B_{56}(CO)_n^-$ (*n* = 1–4) and also found a linear relationship between the chemisorption energies and the number of adsorbed molecules: E_{cse} = 2.47*n* + 0.26 and E_{cse} = 1.61*n* + 0.08 for C_2H_4 (*SI Appendix*, Fig. S7C) and CO (*SI Appendix*, Fig. S7D), respectively.

Mechanisms of CO_2 Chemisorption on B_{56}^-. The most remarkable observation in the chemisorption study is the activation of CO_2 by B_{56}^- (Fig. 1). We explore CO_2 adsorption on the four low-lying isomers of B_{56}^- in Fig. 5 and found that all four isomers can form a $B_{56}(CO_2)^-$ complex at DLPNO-CCSD(T). However, the adsorption energy on the core-shell B@B_{55}^- isomer **7** with a smooth B_{55} shell is only 0.88 eV, whereas the adsorption energies on the GM nest-like **5** (1.33 eV), the second nest-like **6** (1.60 eV), and the bilayer isomer **8** (1.80 eV) are significantly higher. Thus, the formation of the $B_{56}(CO_2)^-$ complex by isomer **7** under ambient condition is expected to be unfavorable thermodynamically and it should account for the unreactive population (43%) of B_{56}^- (Fig. 1C), whereas the nest-like isomers **5** and **6** and the bilayer isomer **8** are responsible for the

reactive population (57%), very similar to the chemisorption of C_2H_4 and CO on B_{56}^-. Furthermore, we find that the CO_2 chemisorption site on the GM nest-like isomer **5** is the exposed top B_3 unit of the B_{12} core (see the 3D structure), the same as the top-adsorption site of C_2H_4 (Fig. 4C). The chemisorption leads to the breaking of one O–C π-bond in O=C=O, forming one C–B σ-bond and one O–B σ-bond with a chemisorption energy of E_{cse} = 1.33 eV (Fig. 5A). The second nest-like isomer **6** favors a bottom-adsorption approach to adsorb CO_2, with an adsorption energy of 1.60 eV. Our calculation shows that the $B_{56}(CO_2)^-$ chemisorption complexes formed by the nest-like isomers **5** and **6** cannot release a CO to form the $B_{56}O^-$ product because of their large reaction barriers of +1.45 eV and +0.46 eV (**TS13** and **TS14** in Fig. 5A), respectively. Surprisingly, the $B_{56}(CO_2)^-$ complex formed by the bilayer isomer **8** can release a CO to form the $B_{56}O^-$ product with an exothermicity of 1.14 eV. The transition state (**TS18**, Fig. 5D) for this reaction is 0.24 eV below the entrance channel. Thus, the bilayer **8** as a minor isomer can react with CO_2 under ambient conditions to form $B_{56}O^-$ + CO and should account for the 9% population of B_{56}^- that reacts with CO_2 to form $B_{56}O^-$.

The structures and low-lying isomers of B_{46}^- and B_{56}^- determined from the PES and theoretical calculations can explain the chemisorption results consistently, providing considerable credence to the core-shell 3D structures of B_{46}^- and the nest-like GM structure for B_{56}^-. The existence of multiple isomers hinted in the PES data are well corroborated by the chemisorption studies.

Chemical Bonding in the Core-Shell Structure of B_{46}^- and the Nest-Like B_{56}^-. To better comprehend the structures and stability of the GM structures of $B_2@B_{44}^-$ (**1**) and $B_{12}@h\text{-}B_{44}^-$ (**5**), we use the adaptive natural density partitioning (AdNDP) approach (29) to decipher the bonding patterns of these remarkable 3D clusters. The low symmetry and complicated architectures of these open-shell 3D clusters make it quite challenging for the bonding analyses. For simplicity, we used the closed-shell C_2 $B_2@B_{44}$ neutral optimized from the C_2 $B_2@B_{44}^-$ GM isomer **1** and the C_1 $B_{12}@h\text{-}B_{46}^{2-}$ closed-shell dianion obtained from the C_1 $B_{12}@B_{44}^-$ GM isomer **5**. As shown in Fig. 6A, the bottom B atom of the B_2 core in $B_2@B_{44}$ (**1**) forms two equivalent two-center-two-electron (2c-2e) σ bonds with two hexa-coordinate B centers in two concave hexagons, the top B atom forms two 3c-2e σ bonds each involving one hexa-coordinate B center in a concave hexagon and one pentacoordinate B center in a neighboring concave pentagon, while the B–B interaction in the B_2 core is reflected in a 4c-2e σ bond involving two equivalent pentacoordinate B centers in two concave pentagons on the equator. There exist six 2c-2e σ bonds symmetrically distributed around two unfilled hexagons, fifty-two 3c-2e σ bonds on the filled hexagons and pentagons on the B_{44} shell. The remaining twelve valence electrons are distributed in two 9c-2e π bonds on the top and bottom and four 11c-2e π bonds on the equator in an overall symmetry of C_2. The occupation numbers (ONs) for all AdNDP bonding elements appear to be slightly smaller than the ideal value of 2 |e|, indicating that there exists more electron delocalization. Nevertheless, the AdNDP analyses give an intuitive bonding picture, consistent with the complicated 3D structure of the core-shell GM **1** for the B_{46}^- cluster.

The bonding in the C_1 $B_{12}@B_{44}^{2-}$ (Fig. 6B) is more straightforward to understand: the bonding elements of the icosahedral B_{12} core and the B_{44} half-shell can be readily recognized. For the half-shell, we find one 2c-2e σ bond at the bottom between the two neighboring unfilled pentagons, seven 2c-2e σ bonds between the B_{12} core and the half-shell (four at the interface and three between the bottom B_3 triangle of the B_{12} core and the three center B atoms from three concave hexagons on the half shell), three 3c-2e σ bonds (one on the top B_3 triangle of the B_{12} core and

two at the interface between the B_{12} core and the half-shell), fifty-nine 3c-2e σ bonds distributed on the surface of the half-shell, and two 7c-2e π bonds over two filled hexagons at the back of the B_{44} half-shell. Most significantly, the remaining twenty-six valence electrons are totally delocalized in thirteen 12c-2e bonds on the half-covered icosahedral B_{12} core matching the *n*+1 Wade's rule (*n* = 12) for polyhedral borane compounds (30). Since these are completely delocalized bonds over the B_{12} core, the AdNDP bonding elements are similar to the corresponding molecular orbitals (MOs). The 13 pairs of electrons can be viewed as filling one 1S MO, three 1P MOs, five 1D MOs, and four 1F MOs. The $1S^21P^61D^{10}1F^8$ electron configuration is exactly the same as the B_{12} units in α-rhombohedral boron (α-B_{12}) or in the icosahedral $B_{12}H_{12}^{2-}$ borane (31, 32). It is also analogous to that of the superatomic icosahedral Al_{13}^- ($1S^21P^61D^{10}2S^21F^{14}2P^6$) in the jellium model (33) or the highly stable bilayer Ag_{13}^- cluster ($1S^21P^42S^21D^4$) due to crystal field splitting (34). The high stability of the icosahedral B_{12} unit originates from the electron delocalization or spherical aromaticity of the nest-like configuration, as evidenced by the large calculated negative nucleus-independent chemical shift of –49.2 ppm at the center of the B_{12} core (35). We also analyzed the bonding of the second nest-like C_s $B_{12}@B_{44}^-$ (**6**) using the closed-shell C_s $B_{12}@B_{44}^{2-}$ (*SI Appendix*, Fig. S8) and found that the bonding in the B_{12} core is similar to that in the GM C_1 $B_{12}@B_{44}^{2-}$.

Discussion

In bulk boron allotropes, the B_{12} icosahedral building blocks facilitate electron delocalization to compensate the electron deficiency of elemental boron. The different arrangements of the B_{12} units, along with interstitial boron atoms, give rise to the structural complexities observed in bulk boron. In small boron clusters, planar structures (*SI Appendix*, Fig. S1) provide the most favorable pathway for electron delocalization and sharing. As cluster size increases, the additional bonding available in 3D structures make them more energetically competitive and thus more favorable. Combined photoelectron spectroscopy and chemisorption experiments unequivocally confirm that the $B_2@B_{44}^-$ (**1**) core-shell structure is the global minimum. While cage structures appear at B_{39}^- and B_{40}^- (12, 13), the core-shell B_{46}^- cluster represents the onset of the transition to true 3D structures. The B_2 core in $B_2@B_{44}^-$ (**1**) is reminiscent of the interstitial B_2 dumbbells in the partially ionic γ-B_{28} form of boron (36), and the single B atom core in the core-shell C_1 $B@B_{45}^-$ (**2**, **3**, and **4**) resembles the interstitial B atoms in α-tetragonal boron (37).

The appearance of the iconic B_{12} core in both the GM C_1 $B_{12}@B_{44}^-$ (**5**) and the second lowest-lying isomer C_s $B_{12}@B_{44}^-$ (**6**), which are the smallest boron clusters containing a B_{12} core (20, 23), marks the onset of bulk-like features in boron nanoclusters. The fact that the half-covered B_{12} core in B_{56}^- obeys the *n*+1 Wade's rule in bonding patterns indicates local spherical aromaticity, which accounts for the high stability of the nest-like structures at this cluster size. The structural transition from B_{46}^- to B_{56}^- does not appear to be smooth, since the B_{48}^- cluster is known to adopt a bilayer structure (24) and the B_x^- (*x* = 47–54) clusters in between are not reactive (Fig. 1A). Consistent with the complexity of bulk boron allotropes, size-selected boron clusters also exhibit remarkable structural diversity. The complexity and unpredictability of boron at the nanoscale suggest there may exist even more fascinating boron clusters as size increases. The unprecedented activation of CO_2 by the B_{56}^- cluster provides critical insights for designing boron nanoclusters with tailored properties. These findings serve as important milestones in understanding the structural evolution of boron nanoclusters and their potential applications in chemistry and materials science.

Materials and Methods

Detailed information regarding all the experimental and theoretical methods is provided in the *SI Appendix*. Briefly, the chemisorption experiment was conducted using a time-of-flight (TOF) mass spectrometer equipped with a laser vaporization cluster source, a quadrupole mass filter, and a linear ion trap reactor. Negatively charged boron clusters generated from laser vaporization of a ^{11}B-enriched target were directed into the linear ion trap, where the clusters were confined and thermalized before being exposed to reactant gases. The reaction products were detected by a reflectron TOF mass spectrometer. The PES experiment was performed using a magnetic-bottle apparatus equipped with a laser vaporization cluster source and a TOF mass spectrometer. Size-selected clusters were decelerated before photodetachment by a laser beam. The photoelectrons were analyzed by a magnetic-bottle TOF electron analyzer. Global minimum searches for the B_{46}^- and B_{56}^- clusters were carried out using the stochastic surface walking method, as well as manual structural constructions. Independent structural searches were further conducted using the Tsinghua global minimum approach based on the basin hopping algorithm. Density functional theory calculations were done at the PBE0 level to fully optimize the low-lying isomers of the clusters. Single-point calculations were performed on the low-lying isomers using the high level domain-based local pair natural orbital coupled-cluster approach with single and double excitations and perturbative triples corrections [DLPNO-CCSD(T)] implemented in the ORCA program.

Acknowledgments

The experimental work was supported by the U.S. National Science Foundation (CHE-2403841 to L.S.W.) and the National Natural Science Foundation of China (Grant 22003034 to Q.C.). The theoretical work was supported by the National Natural Science Foundation of China (Grants 22373061 and 92461303 to S.D.L and Grant 22173069 to G.F.W.).

References

1. H. W. Kroto, J. R. Heath, S. C. O'Brien, R. F. Curl, R. E. Smalley, C_{60}: Buckminsterfullerene. *Nature* **318,** 162-163 (1985).
2. S. Iijima, Helical microtubules of graphitic carbon. *Nature* **354,** 56-58 (1991).
3. K. S. Novoselov *et al*., Electric field effect in atomically thin carbon films. *Science* **306,** 666-669 (2004).
4. W. D. Knight et al., Electronic shell structure and abundances of sodium clusters. *Phys. Rev. Lett.* **52,** 2141-2143 (1984).
5. M. Walter, *et al.*, A unified view of ligand-protected gold clusters as superatom complexes. *Proc. Natl Acad. Sci.* **105,** 9157-9162 (2008).
6. H. Prinzbach *et al*. Gas-phase production and photoelectron spectroscopy of the smallest fullerene, C_{20}. *Nature* **407,** 60-63 (2000).
7. M. A. White, A. B. Cerqueira, A. A. Whitman, M. B. Johnson, T. Ogitsu, Determination of phase stability of elemental boron. *Angew. Chem. Int. Ed*. **54**, 3626-3629 (2015).
8. A. P. Sergeeva *at al*., Understanding boron through size-selected clusters: Structure, chemical bonding, and fluxionality. *Acc. Chem. Res*. **47**, 1349-1358 (2014).
9. L. S. Wang, Photoelectron spectroscopy of size-selected boron clusters: From planar structures to borophenes and borospherenes. *Int. Rev. Phys. Chem*. **35**, 69-142 (2016).

10. T. Jian *et al*., Probing the structures and bonding of size-selected boron and doped-boron clusters. *Chem. Soc. Rev*. **48**, 3550-3591 (2019).
11. H. Bai *et al*., Planar B_{41}^- and B_{42}^- clusters with double-hexagonal vacancies. *Nanoscale* **11**, 23286-23295 (2019).
12. H. J. Zhai *et al*., Observation of an all-boron fullerene. *Nat. Chem*. **6**, 727-731 (2014).
13. Q. Chen *et al*., Experimental and theoretical evidence of an axially chiral borospherene. *ACS Nano* **9**, 754-760 (2015).
14. Z.A. Piazza *et al*., Planar hexagonal B_{36} as a potential basis for extended single-atom layer boron sheets. *Nat. Commun*. **5**, 3113 (2014).
15. A. J. Mannix *et al*., Synthesis of borophenes: Anisotropic, two-dimensional boron polymorphs. *Science* **350**, 1513-1516 (2015).
16. B. Feng *et al.,* Experimental realization of two-dimensional boron sheets. *Nat. Chem.* **8**, 563-568 (2016).
17. D. L. V. K. Prasad, E. D. Jemmis, Stuffing improves the stability of fullerenelike boron clusters. *Phys. Rev. Lett*. **100**, 165504 (2008).
18. H. Li *et al*., Icosahedral B_{12}-containing core-shell structures of B_{80}. *Chem. Commun*. **46**, 3878-3880 (2010).
19. S. De *et al*., Energy landscape of fullerene materials: A comparison of boron-to-boron nitride and carbon. *Phys. Rev. Lett*. **106**, 225502 (2011).
20. F. Li *et al*., B_{80} and $B_{101\text{-}103}$ clusters: Remarkable stability of the core-shell structures established by validated density functionals. *J. Chem. Phys*. **136**, 074302 (2012).
21. M. Zhang, H. G. Lu, S. D. Li, B_{111}, B_{112}, B_{113}, B_{114}: The most stable core-shell borospherenes with icosahedral B12 core at the center exhibiting superatomic behaviors. *Nano Res*. **14**, 4719-4724 (2021).
22. L. Sai, X. Wu, N. Gao, J. Zhao, R. B. King, Boron clusters with 46, 48, and 50 atoms: Competition among the core–shell, bilayer and quasi-planar structures. *Nanoscale* **9**, 13905-13909 (2017).
23. X. Wu *et al*., Pivotal role of the B_{12}-core in the structural evolution of B_{52}-B_{64} clusters. *Nanoscale* **15**, 10430-10436 (2023).
24. W. J. Chen *et al*., B_{48}^-: A bilayer boron cluster. *Nanoscale* **13**, 3868-3876 (2021).
25. E. Oger *et al*., Boron cluster cations: Transition from planar to cylindrical structures. *Angew. Chem. Int. Ed*. **46**, 8503-8506 (2007).
26. R. N. Yuan *et al*., Observation of aromatic $B_{13}(CO)_n^+$ (n = 1−7) as boron carbonyl analogs of benzene. *J. Am. Chem. Soc.* **146**, 31464-31471 (2024).
27. S. D. Huang, C. Shang, X. J. Zhang, Z. P. Liu, Material discovery by combining stochastic surface walking global optimization with a neural network. *Chem. Sci.* **8**, 6327−6337 (2017).
28. Q. Q. Yan, L. Pei, S. D. Li, Predicting bilayer B_{50}, B_{52}, B_{56}, and B_{58}: Structural evolution in bilayer B_{48}–B_{72} clusters. *J. Mol. Model.* **27**, 364 (2021).
29. D. Y. Zubarev, A. I. Boldyrev, Developing paradigms of chemical bonding: Adaptive natural density partitioning. *Phys. Chem. Chem. Phys.* **10**, 5207-5217 (2008).
30. K. Wade, The structural significance of the number of skeletal bonding electron-pairs in carboranes, the higher boranes and borane anions, and various transition-metal carbonyl cluster compounds. *Chem. Commun.* 792-793 (1971).
31. W. H. Eberhardt, B. L. Crawford Jr, W. N. Lipscomb, The valence structure of the boron hydrides. *J. Chem. Phys*. **22**, 989-1001 (1954).

32. H. C. Longuet-Higgins, M. de V. Roberts, The electronic structure of an icosahedron of boron atoms. *Proc. Roy. Soc. (London)* **A230**, 110-119 (1955).
33. X. Li, H. Wu, X. B. Wang, L. S. Wang, *s-p* hybridization and electron shell structures in aluminum clusters: A photoelectron spectroscopy study. *Phys. Rev. Lett*. **81**, 1909-1912 (1998).
34. Y. Jia and Z. Luo, Thirteen-atom metal clusters for genetic materials, *Coord. Chem. Rev.* **400**, 213053 (2019).
35. P. v. R. Schleyer, C. Maerker, A. Dransfeld, H. Jiao, N. J. R. van E. Hommes, Nucleus-independent chemical shifts: A simple and efficient aromaticity probe. *J. Am. Chem. Soc.* **118**, 6317−6318 (1996).
36. A. R. Oganov *et al*., Ionic high-pressure form of elemental boron. *Nature* **457**, 863-867 (2009).
37. N. Uemura, K. Shirai, H. Eckert, J. Kunstmann, Structure, nonstoichiometry, and geometrical frustration of a-tetragonal boron. *Phys. Rev. B* **93**, 104101 (2016).

Figures

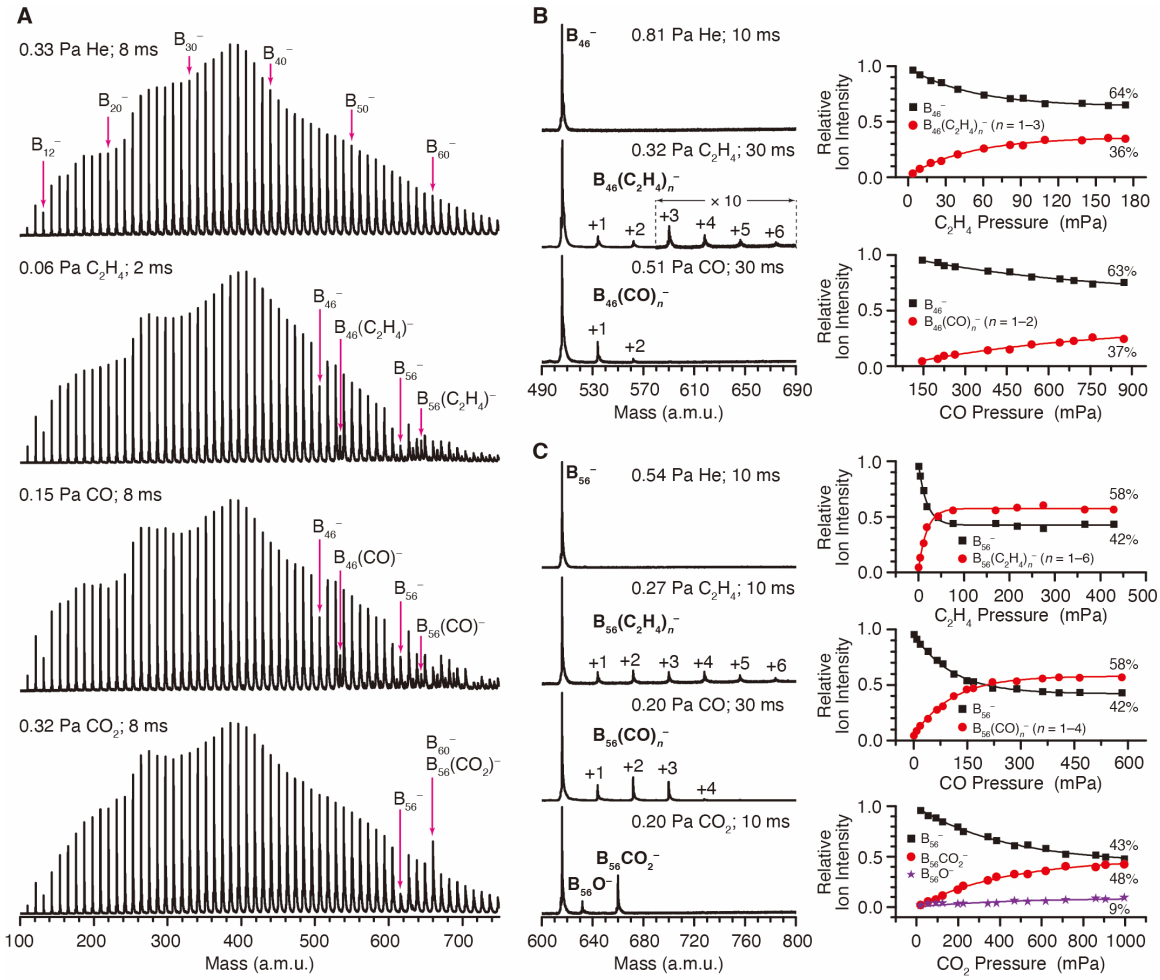

Figure 1. Chemisorption Studies. (A) Mass spectra of the B_x^- clusters (x = 10–68) and their chemisorption reactions with C_2H_4, CO, and CO_2. (B) Mass-selected B_{46}^- and its reactions with C_2H_4 and CO, with the mass signals of $B_{46}(C_2H_4)_n^-$ (n = 3-6) enlarged by ten times. (C) Mass-selected B_{56}^- and its reactions with C_2H_4, CO, and CO_2. The reactant gas pressures (Pa) and reaction times (ms) are indicated. The relative intensities of the reactant and product cluster ions are given for the reactions of B_{46}^- + C_2H_4, B_{46}^- + CO, B_{56}^- + C_2H_4, B_{56}^- + CO, and B_{56}^- + CO_2. In the kinetic studies on the right side of (B) and (C), the dots are experimental data and the lines are least-squares fittings based on the approximation of pseudo-first-order reaction mechanisms, with the corresponding extrapolated percentage contributions to the overall mass intensities indicated. Both B_{46}^- and B_{56}^- exhibit special adsorption reactivities with C_2H_4 and CO among the B_x^- clusters, while B_{56}^- is unique in its reactivity with CO_2.

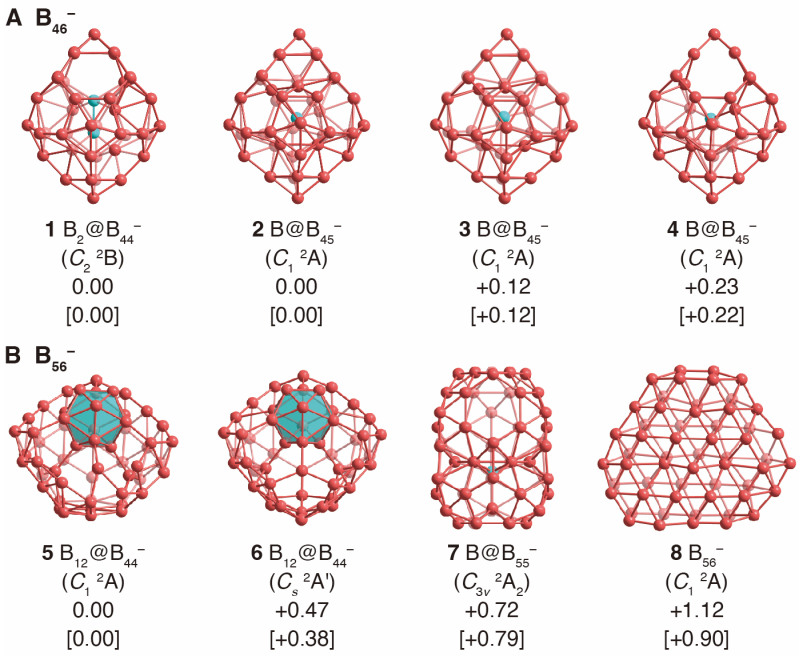

Figure 2. Optimized structures of the four lowest-lying isomers of (A) B_{46}^- and (B) B_{56}^- at the PBE0 level. Their overall relative electronic energies (ΔE/eV) at 0 K and Gibbs free energies (ΔG/eV, in square brackets) at 298 K are given at the DLPNO-CCSD(T) level. The B_2 core in the core-shell C_2 B_{46}^- ($B_2@B_{44}^-$, **1**), the single B core in the core-shell C_1 B_{46}^- ($B@B_{45}^-$, **2**, **3,** and **4**) and the C_{3v} B_{56}^- ($B@B_{55}^-$, **7**), and the icosahedral B_{12} core in the nest-like C_1 B_{56}^- ($B_{12}@h$-B_{44}^-, **5**) and C_s B_{56}^- ($B_{12}@h$-B_{44}^-, **6**) are highlighted in blue.

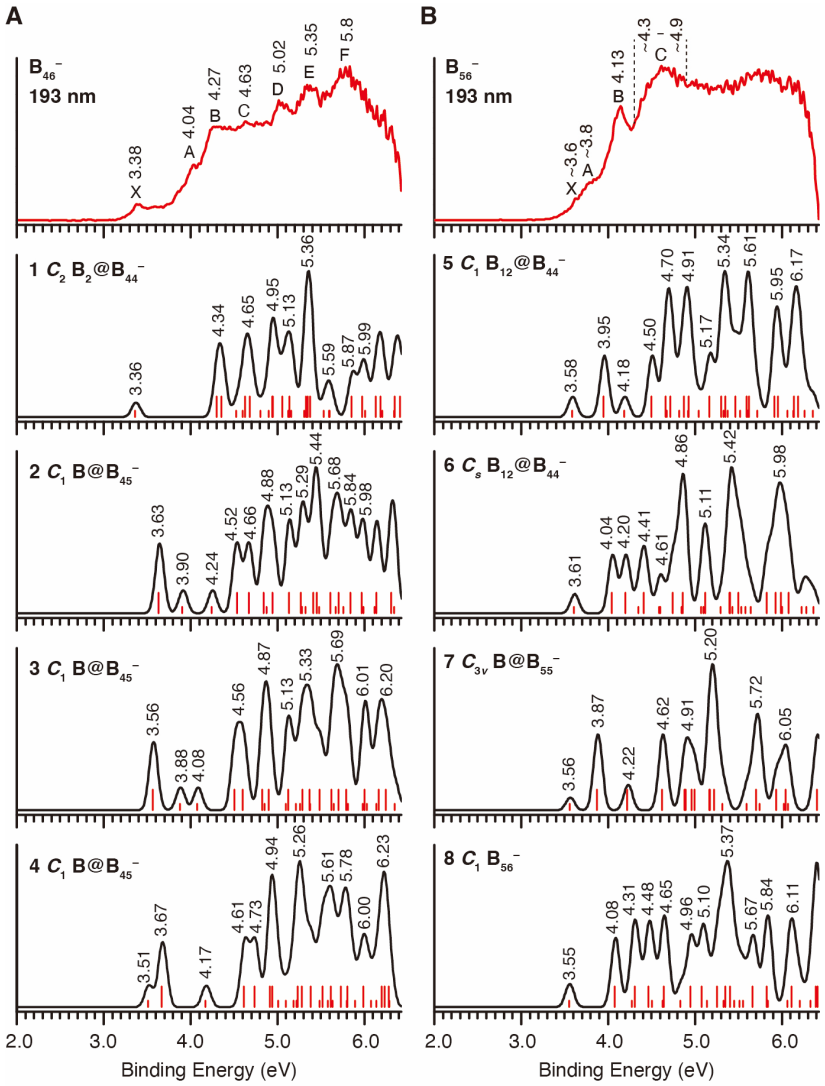

Figure 3. The measured 193 nm photoelectron spectra of (A) B_{46}^- and (B) B_{56}^- compared with the simulated spectra of their four lowest-lying isomers at the PBE0/6-311+G(d) level. The short and long red vertical lines represent the singlet and triplet final states, respectively. Each detachment channel is fitted with a unit area Gaussian of 0.1 eV FWHM to produce the simulated spectra. An area ratio of 3 to 1 was used for the triplet and singlet final states. Spectral features are labeled and the VDEs are given in eV. For the experimental spectrum of B_{46}^-, the bands X, B, C, D, and E are well reproduced by the simulated spectrum of the GM isomer **1**, while isomer **2** can account for the features between bands X and B, including band A. Isomer **3** gives similar simulated features as isomer **2**; its contributions should be minor, in present at all, according to the chemisorption data. The predicted first VDEs of the four lowest-lying isomers of B_{56}^- are all in agreement with the X band (~3.6 eV) observed in the experimental spectrum. The simulated spectra of isomers **5** and **7** exhibit relatively smaller HOMO-LUMO gaps, with their second detachment bands corresponding to band A of B_{56}^-. The strong peak B could have contributions from the third detachment bands of isomers **5** and **7** and the second detachment bands of isomer **8**. Isomer **6** of B_{56}^- gives similar simulated spectral features as those of isomer 5 and it could also contribute to the observed spectrum. Also see Table S2.

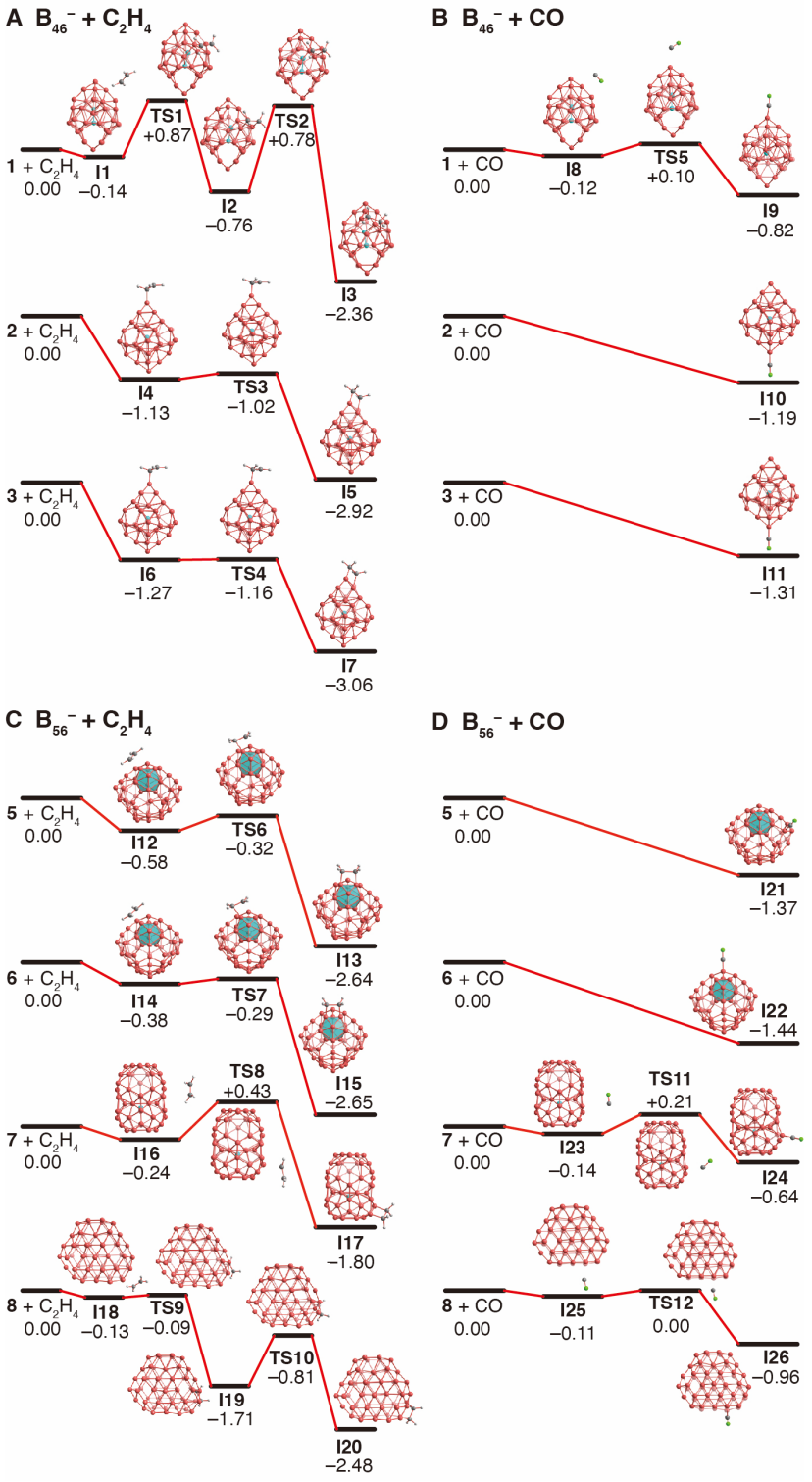

Figure 4. Chemisorption mechanisms by C_2H_4 and CO on the three low-lying Isomers of B_{46}^- and four low-lying isomers of B_{56}^-, with the energy barriers indicated in eV at DLPNO-CCSD(T). (A) $B_{46}^- + C_2H_4$. (B) $B_{46}^- + CO$. (C) $B_{56}^- + C_2H_4$. (D) $B_{56}^- + CO$.

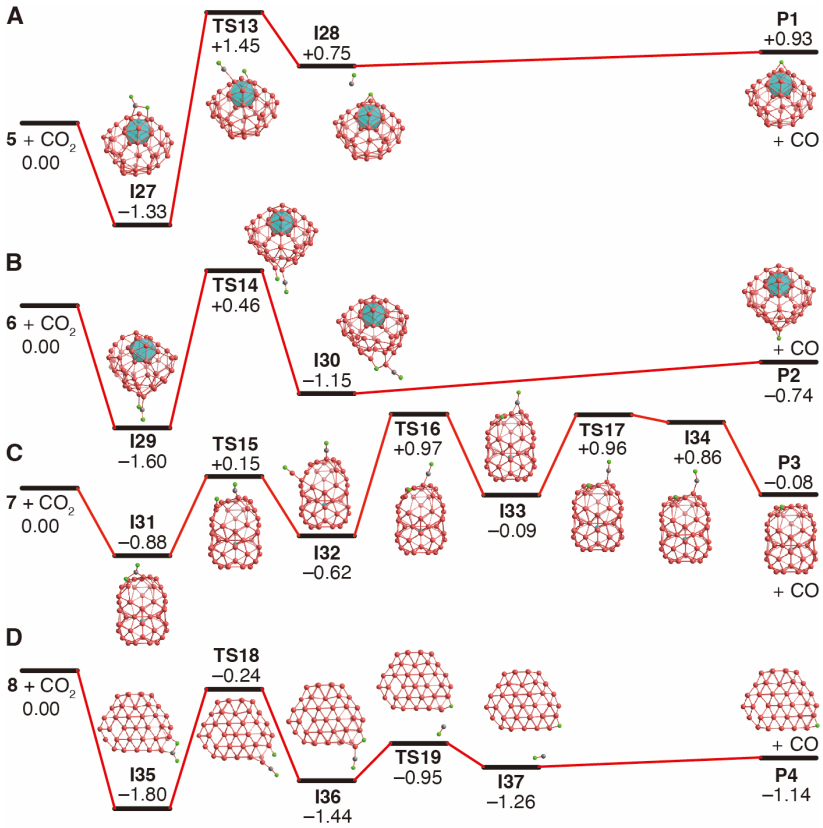

Figure 5. CO_2 Chemisorption and CO-Desorption Mechanisms on B_{56}^-, with the energy barriers indicated in eV at DLPNO-CCSD(T). (A) On the GM nest-like B_{12}@*h*-B_{44}^- isomer **5**. (B) On the second nest-like B_{12}@*h*-B_{44}^- isomer **6**. (C) On the core-shell B@B_{55}^- isomer **7**. (D) On the bilayer isomer **8.** Only the CO_2 complex of the bilayer isomer **8** (**I37**) can release a CO to form the $B_{56}O^-$ product. The CO_2 complexes of the nest-like isomer **5** (**I27**), nest-like isomer **6** (**I29**), and core-shell isomer **7** (**I31**) exhibit large energy barriers and endothermicities for the release of CO to form $B_{56}O^-$.

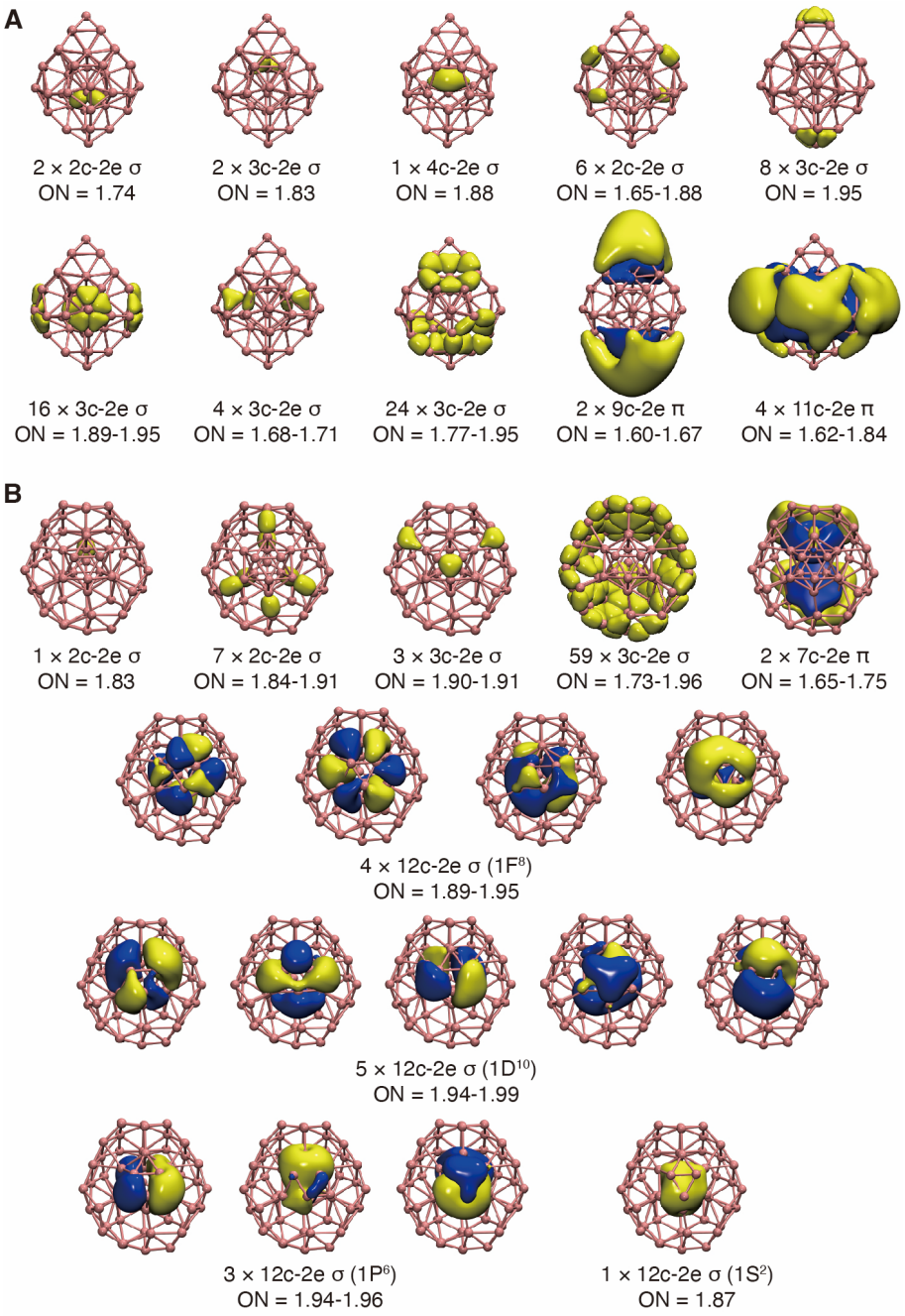

Figure 6. AdNDP chemical bonding analyses. (A) For the closed-shell neutral core-shell C_2 $B_2@B_{44}$ structure optimized from the GM $B_2@B_{44}^-$ structure **1**. (B) For the closed-shell nest-like C_1 $B_{12}@B_{44}^{2-}$ species obtained from the GM nest-like $B_{12}@B_{44}^-$ structure **5**. The occupation numbers (ONs) are given in |e|. The half-covered B_{12} icosahedral core in $B_{12}@B_{44}^{2-}$ follows the (n + 1) Wade's rule, rendering spheric aromaticity and extra stability to the nest-like GM structure.